Journal of Alloys and Compounds 545 (2012) 190–199

Contents lists available at SciVerse ScienceDirect

Journal of Alloys and Compounds

journal homepage: www.elsevier.com/locate/jalcom

Some physical investigations of $AgInS_{2-x}Se_x$ thin film compounds obtained from $AgInS_2$ annealed in seleneide atmosphere

D. Gherouel [a], I. Gaied [b], K. Boubaker [a,*], N. Yacoubi [b], M. Amlouk [a]

[a] Unité de Physique des Dispositifs à Semi-conducteurs, Faculté des Sciences de Tunis, Tunis El Manar University, 2092 Tunis, Tunisia
[b] Institut Préparatoire Aux Etudes d'Ingénieurs de Nabeul, Merazka, 8000 Nabeul, Tunisia

ARTICLE INFO

Article history:
Received 5 July 2012
Received in revised form 30 July 2012
Accepted 30 July 2012
Available online 19 August 2012

Keywords:
$AgInS_{2-x}Se_x$
Annealing temperature
Mirage effect
Urbach tailing
Amlouk–Boubaker opto-thermal expansivity

ABSTRACT

This work deals with the preparation of $AgInS_{2-x}Se_x$ from $AgInS_2$ (AIS) sprayed thin films which treated under seleneide atmosphere during 1 h at various temperatures (400, 450 and 500 °C). Previously elaborated $AgInS_2$ compound, which has been conceived as an absorber layer in the SnO_2:F/$AgInS_2$ (p)/Al Schottky diode, has presented some generation–recombination deficiencies and tunneling effects. XRD analysis shows the incorporation of Se element in the $AgInS_2$ matrix especially for use of 450 °C as heat temperature. The optical band gap calculated from transmittance and reflectance spectra of the above samples show the effect of annealed temperature on the band gap energy. The refractive index and extinction coefficient of the differently sample of $AgInS_{2-x}Se_x$ thin films have been reached through their transmission and reflectance spectra on a wide range of wavelengths. The surface topography and the roughness parameters of $AgInS_{2-x}Se_x$ thin films had been studied by AFM. Finally, thermal conductivity was determinate by the mirage effect. This thermal property was decreased by the annealed temperatures.

1. Introduction

I–III–VI_2 compounds are direct energy-gap semiconductors and have long been a subject of various researches because of their specials physical properties such as thermal and optical properties. Their large absorption coefficient above 10^5 cm^{-1} and its band gap energy between 1.0 and 1.97 eV at room temperature [1–3] allow them to be good candidates for use in solar cell technologies [3–11]. Indeed, high conversion efficiencies for polycrystalline CIGS based solar cells have been significantly reached and the best cell of 20% is now reported [2].

$AgInS_2$ ternary material is unique among I–III–VI_2 compounds as it can exist in two ordered phases namely chalcopyrite and orthorhombic [11]. The orthorhombic modification of $AgInS_2$ is pseudo-würtzite, just as the chalcopyrite structure is pseudo-zincblende. The orthorhombic form is stable at high temperature ($T > 620$ °C) and the chalcopyrite form is stable at low temperature ($T < 620$ °C) [8]. Nevertheless, $AgInSe_2$ has chalcopyrite structure which is an ordered superstructure of zincblende.

To meet the requirements in different application domains, AIS can be doped with a variety of ions [9–12]. Several techniques such as organometallic chemical vapor deposition (MOCVD) [13], chemical vapor transport (CVT) [14], laser ablation [15] and magneto-sputtering [16] have been used to prepare thin films of these types of I–III–VI_2 compounds.

These techniques are generally so expensive hence the need for a simple, easy and less expensive technique is in demand. For these reasons, we have used the spray pyrolysis technique [17–20] because it can be easily adapted for film of large area production, and it allows us to have thin films with size grain that we can control by the precursors concentrations.

The present paper reports the effect of vacuum annealing in the presence of selenium at different temperatures of AIS spray thin films on structural, optical and thermal properties of $AgInS_{2-x}Se_x$ thin films. The main aim of this study is to enhance the previously obtained compound $AgInS_2$ compounds [10] by minimizing the presence of other than the chalcopyritic phase and shifting band gap energy E_g toward 1.5 eV, value which matches better the maximum of solar spectrum conversion.

2. Experiment

2.1. Synthesis of $AgInS_2$

$AgInS_2$ thin films were first prepared at a glass substrate temperature of 420 °C using an aqueous solution which contains silver acetate ($AgCH_3CO_2$), thiourea ($SC(NH_2)_2$) and indium chloride ($InCl_3$) as precursors. The precursor's

* Corresponding author.
E-mail addresses: mmbb11112000@yahoo.fr, math_physics2008@yahoo.fr (K. Boubaker).

0925-8388/$ - see front matter © 2012 Elsevier B.V. All rights reserved.
http://dx.doi.org/10.1016/j.jallcom.2012.07.148

concentrations are $[Ag^+]/[In^{3+}] = 1.3$ and $[S^{2-}]/[In^{3+}] = 5$. Molar ratios were prepared by mixing appropriate volumes of silver acetate 10^{-2} M. indium chloride 1.3×10^{-2} M. and thiourea 5×10^{-2} M. This protocol is considered as optimal condition for preparing such a p-type compound [4,5]. The carrier gas was nitrogen (pressure ≈ 0.35 bar) through a 0.5 mm-diameter nozzle. The nozzle-to-substrate plane distance was fixed at the optimal value of 27 cm as demonstrated earlier, for the same disposal, by Boubaker et al. [20]. During the whole deposition process, precursor mixture flow rate was approximately 4 mL/min.

In the second step, $AgInS_2$ sprayed thin films are annealed at three different temperatures (400 °C, 450 °C and 500 °C) with 10 mg of selenium in pyrex sealed vacuum tube for 1 h.

2.2. Characterization techniques

The structural characterization of $AgInS_{2-x}Se_x$ thin films were carried out using an X-ray diffractometer (XRD X-ray diffraction spectra were obtained by means of a Philips (PW1429) system using two Cu Kα monochromatic radiations ($\lambda_1 = 1.54050$ Å, $\lambda_2 = 1.54438$ Å). The optical measurements of the transmittance and the reflectance were carried out in the wavelength range 300–1800 nm using unpolarized light by means of a spectrophotometer (Shimadzu UV 3100S). An integrating sphere (LISR 3200) coupled to the spectrophotometer was used for these measurements. Film surfaces were analyzed by means of AFM (VEECO digital instrument 3A) in contact mode. Finally, Thermal properties were investigated by the effect mirages.

3. Achieved analyses and discussion

3.1. XRD analyses

The crystalline properties of $AgInS_2$ unannealed and annealed thin films under Se atmosphere were investigated by the XRD measurement. Fig. 1 shows the XRD patterns of the different samples. The diffractogram of unannealed film shows in addition to (112) principal orientation the presence of others peaks such as (200), (220) and (312) corresponding to chalcopyrite tetragonal structure according to JCPDS 75-0118 cards. It also contains peaks (111) and (022) related to Ag_2S binary phase and (024) peak which corresponds to In_2S_3 phase binary as well as the presence of (131) peak assigned to $AgInS_2$ orthorhombic phase which induces a subsequent poor crystallinity.

In Table 1, we summarized the reticular distance of (112) principal orientation and lattice constant as a function of the annealed temperature with Se. We note that d112 increases from value of $AgInS_2$ and reached $AgInSe_2$ one. This shift regarding d112 peak is probably due to the incorporation of Se element in $AgInS_2$ matrix.

These results depict that the formation reaction of $AgInS_2$–Se material goes on slowly and may require a thermodynamic activation with the annealing temperatures. Thus, for annealed films at three different temperatures (400, 450 and 500 °C) were mark the appearance of novel diffraction peaks having other reticular distances (d1 = 3.302 Å, d2 = 3.437 Å and d3 = 3.443 Å) which are not belonged to $AgInS_2$ or $AgInSe_2$ materials. On the contrary, for b, c and d samples, the undesirable binaries (Ag_2S and In_2S_3) do not appear in the XRD spectra. Moreover, the (112) direction remains very strong and the full-width at half-maximum (FWHM), which is very small (less than 0.2) shows a good crystal in estate of all films, Table 2. This phenomenon concerning the shift in the reticular distance can be explained by the formation of the quaternary compound and the incorporation of Se that comes via this annealing process in the place of sulfur in the polycrystalline matrix. It is obviously noted that these lattice constant (a and c) of the tetragonal structure values remain higher than the AgInS2 ($a = 5.816$ Å and $c = 11.17$ Å) (JCPDS 75-0117) and lower than $AgInSe_2$ ($a = 6.090$ Å and $c = 11.670$ Å) (JCPDS 75-0118).

In the same line, the result regarding the calculation of the grain size and the micro stain and the dislocation shows strong variations of these parameters in terms of the treatment, Table 1. Indeed, these parameters lead to an improvement of the cristanillity of AgInSSe films. We can also notice that the 450 °C as annealed temperature was an appropriate temperature giving high crystallite size and less dislocation and the microstrain.

Consequently, this Se treatment leads to the formation of $AgInS_{2-x}Se_x$ quaternary compounds.

Moreover, the texture coefficient (TC) which indicates the maximum preferred orientation (112). TC(hkl) values have been calculated from X-ray data, using the following formula:

$$TC_{(hkl)} = \frac{I(hkl)/I_0(hkl)}{N^{-1}\sum I(hkl)/I_0(hkl)} \quad (1)$$

where $I_{(hkl)}$ is the measured relative intensity of (hkl) plane, $I_o(hkl)$ is the standard intensity of the same plane taken from the JCPDS card already mentioned, and N is the reflection number.

$TC_{(hkl)}$ calculated values of the different sample are gathered in Table 1.

The interplanar spacing d_{hkl} values of these thin films were also calculated by using Bragg equation:

$$2d_{hkl}\sin\theta = n\lambda \quad (2)$$

Both lattice parameters a and c for the chalcopyrite tetragonal phase are calculated using the following relation [21–23]:

$$\frac{1}{d_{hkl}^2} = \frac{h^2+k^2}{a^2} + \frac{l^2}{c^2} \quad (3)$$

via (112) and (200) orientations for the simple reason: these two peaks appear in all spectra.

Table 2 summarizes the calculated values of d_{hkl} and lattice parameters of chalcopyrite phase of (AIS) thin films.

At first glance, it can be seen that the interplanar spacing d_{hkl} values In particular d_{112} increase with annealed temperature. This phenomenon shows that selenium element is introduced in $AgInS_2$ matrix to obtain $AgInS_{2-x}Se_x$ quaternary and played an important role in improving the optical and thermal properties of such compound.

On the other hand, the average grain size D values can be estimated via Debye–Scherer formula:

$$D = \frac{k\lambda}{\beta_{1/2}\cos\theta} \quad (4)$$

where k is a constant $k = 0.9$, λ the length of wave $\lambda = 1.5418$ Å, β is the full width at half maximum and θ is the position of strong pick.

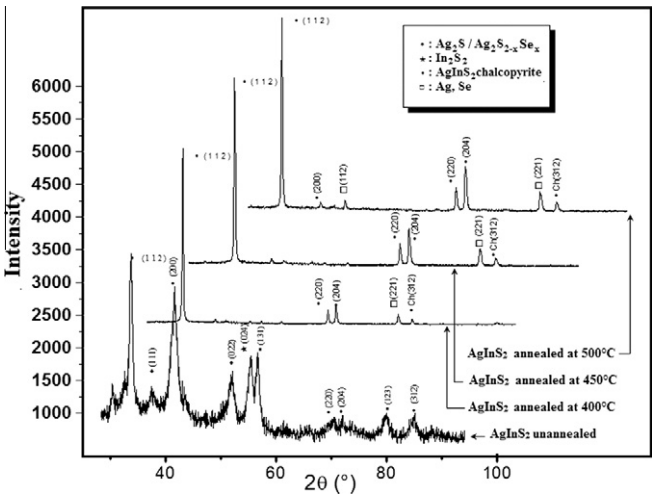

Fig. 1. XRD diagrams of the different samples: ($AgInS_2$ unannealed, annealed at 400 °C, 450 °C and 500 °C).

Table 1
Orientation of composite $AgInS_2$ annealed with selenium (Se) at different temperatures.

Degree orientation	Fiche JCPDS	Ref. [4]	Ref. [5]	$AgInS_2$/glass annealed with selenium (Se)			
				Before annealing	Tr = 400 °C	Tr = 450 °C	Tr = 500 °C
$TC_{(200)}$	0.714	1.04	1.565	2.756	0.210	0.228	0.205
$TC_{(220)}$	0.760	1.102	–	0.369	1.263	1.257	1.128
$TC_{(204)}$	1.428	–	0.652	0.403	2.105	2.171	2.256
$TC_{(312)}$	1.095	0.857	0.780	0.470	0.421	0.342	0.410

Table 2
Crystallographic parameters of thin film $AgInS_2$/glass annealed with Se.

$AgInS_2$ annealed with Se	2θ (°)	d_{112} (Å)	a (Å)	c (Å)	c/a
Before annealing	26.96	3.30	5.78	11.18	1.93
400 °C	25.89	3.437	6.042	11.57	1.914
450 °C	25.87	3.439	6.045	11.58	1.916
500 °C	25.84	3.443	6.045	11.62	1.922

It is clear that the annealing temperature has an effect on the crystallite size which is another argument about the commitment of the element selenium in the $AgInS_2$ matrix.

In fact, the grain size of these films $AgnS_2$ grown by spray pyrolysis method increase with annealed temperature from 62.91 nm to 108.74 nm at 450 °C so, we are suggesting that 450 °C is optimal temperature for the preparation of such a quaternary compound such a finding has been proven through the dislocation density and the optical gap.

The microstrain (ξ), which is an interesting structural parameter of (AIS) thin films, is calculated using the following relation [24]:

$$\xi = \frac{\beta_{1/2}}{4\tan\theta} \tag{5}$$

where, $\beta_{1/2}$ is the full-width at half-maximum of (1 1 2) peak considered as a preferred orientation and θ is the Bragg angle.

Finally, the dislocation density (δ), defined as the length of dislocation lines per unit volume, has been estimated using the equation,

$$\delta = \frac{1}{D^2} \tag{6}$$

δ is the measure of the amount of defects in a crystal. At the first glens, we can see that the values of δ depend on the annealed temperature which indicates that the effect on the crystallization of the (AIS) thin films. We can see that the annealed temperature of 450 °C gives the minimum of the dislocation density which is related to the minimum of structural defects (Table 3).

The variations of the lattice strain and the crystals size shows that the annealing temperature 450 °C is the best annealed temperature.

3.2. Morphological characterization

AFM observations allow us to obtain microscopic information of the surface structure when y increases. Indeed, these micrographs (Figs. 2–5) reveal that all film surfaces are rough. These perturbed surfaces are probably due to very small droplets, resulting from the mini-spray pyrolysis technique, which vaporize above the glass.

Table 3
Variation of the grain size and the strain with annealing temperature.

	$AgInS_2$/glass before annealing	$AgInS_2$/glass annealed with Se		
		Tr = 400 °C	Tr = 450 °C	Tr = 500 °C
D (nm)	62.91	101.94	108.74	100.67
Strain (10^{-3})	2.36	1.51	1.42	1.54
$\delta(10^{13}$ lines/m$^2)$	25.27	9.62	8.46	9.87

AFM observations allow us to obtain microscopic information of the surface structure. Indeed, these micrographs (Fig. 2) reveal that all film surfaces are rough. These perturbed surfaces are probably due to very small droplets, resulting from the mini-spray pyrolysis technique, which vaporize above the glass substrates and condense as microcrystallites with various dimensions (0.1–0.5 mm). We have rounded clusters and the roughness parameter increases from 31.12 nm before annealing to 182.85 nm above 400 °C with Se. the Selenium enters to the thin film. So we obtained other film $AgnS_{2-x}Se_x$, Table 4. This phenomenon may be due to excess selenium in the solid phase. Indeed, as the composition increases, the presence of Ag_2Se after annealing.

3.3. Opto-thermal investigation

The effective absorptivity $\hat{\alpha}$, as defined in precedent studies [25–27], is the mean normalized absorbance weighted by $I(\tilde{\lambda})_{AM1.5}$, the solar standard irradiance:

$$\begin{cases} \hat{\alpha} = \dfrac{\int_0^1 I(\tilde{\lambda})_{AM1.5} \times \alpha(\tilde{\lambda}) d\tilde{\lambda}}{\int_0^1 I(\tilde{\lambda})_{AM1.5} d\tilde{\lambda}} \\ \begin{cases} \lambda \in [\lambda_{min}, \lambda_{max}\,] \Longleftrightarrow \tilde{\lambda} \in [0,1] \\ \lambda_{min} = 300.0 \text{ nm } \lambda_{max} = 1800.0 \text{ nm} \end{cases} \end{cases} \tag{7}$$

where $I(\tilde{\lambda})_{AM1.5}$ is the reference solar spectral irradiance, fitted using the Boubaker polynomials expansion scheme BPES [28–47]:

$$I(\tilde{\lambda}) = \left[\frac{1}{2N_0}\sum_{n=1}^{N_0}\theta_n \cdot B_{4n}(\tilde{\lambda} \times \beta_n)\right],$$

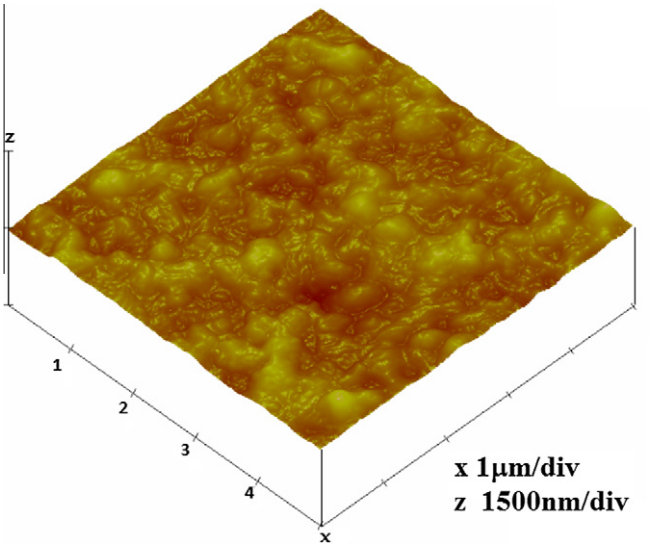

Fig. 2. $AgInS_2$ unannealed.

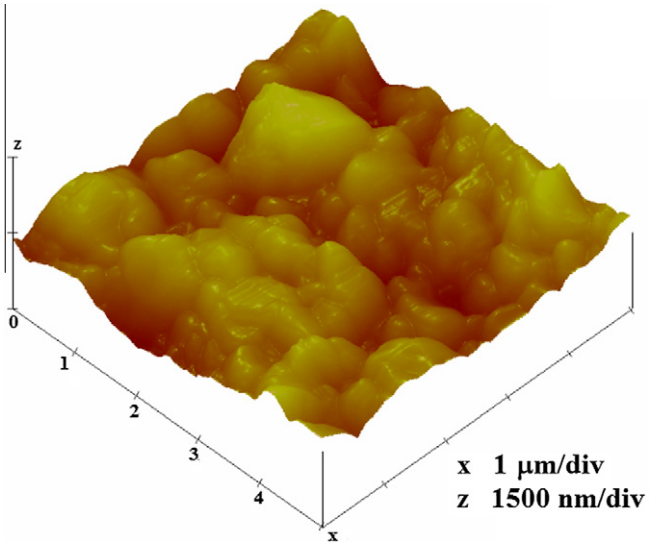

Fig. 3. $AgInS_2$ annealed at 400 °C with Se.

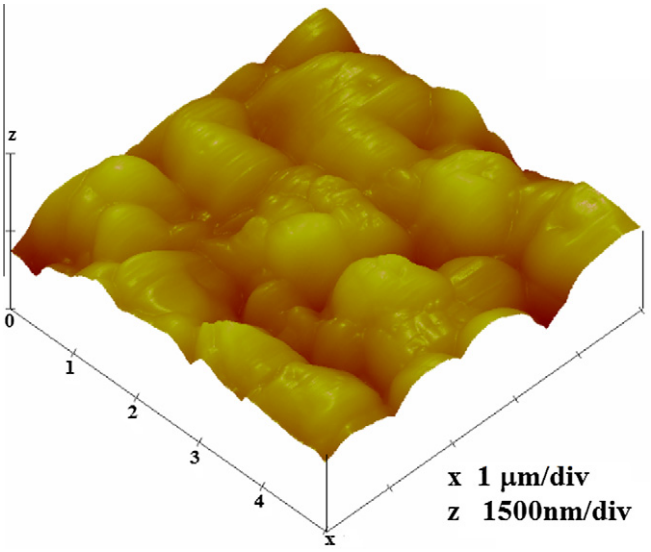

Fig. 4. $AgInS_2$ annealed at 450 °C with Se.

where β_n are the Boubaker polynomials [44–47] B_{4n} minimal positive roots, θ_n are given coefficients, N_0 is a given integer, $\alpha(\tilde{\lambda})$ is the normalized absorbance spectrum and $\tilde{\lambda}$ is the normalized wavelength.

The normalized absorbance spectrum $\alpha(\tilde{\lambda})$ is deduced from the BPES by establishing a set of N experimental measured values of the transmittance-reflectance vector $(T_i(\tilde{\lambda}_i); R_i(\tilde{\lambda}_i))|_{i=1\ldots N}$ vs, the normalized wavelength $\tilde{\lambda}_i|_{i=1\ldots N}$. Then the system (8) is set:

$$\begin{cases} R(\tilde{\lambda}) = \left[\frac{1}{2N_0}\sum_{n=1}^{N_0}\xi_n \times B_{4n}(\tilde{\lambda}\times\beta_n)\right] \\ T(\tilde{\lambda}) = \left[\frac{1}{2N_0}\sum_{n=1}^{N_0}\xi'_n \times B_{4n}(\tilde{\lambda}\times\beta_n)\right] \end{cases} \quad (8)$$

where β_n are the 4n-Boubaker polynomials B_{4n} minimal positive roots [35–45], N_0 is a given integer and ξ_n and ξ'_n are coefficients determined through the Boubaker polynomials expansion scheme BPES.

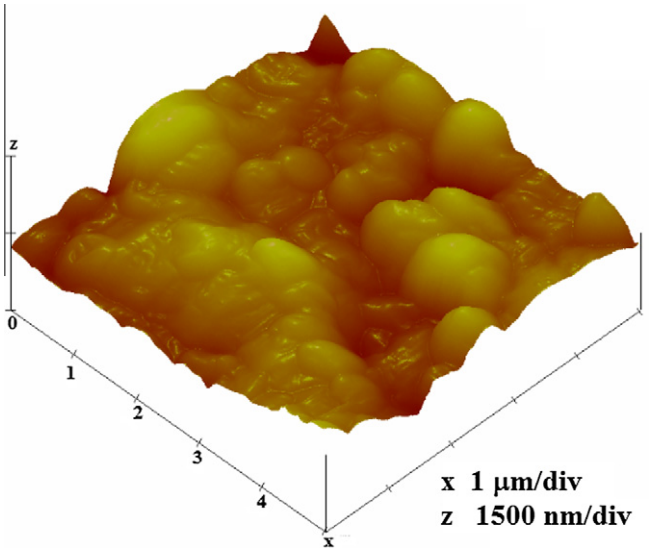

Fig. 5. $AgInS_2$ annealed at 500 °C with Se.

Table 4
Increasing of roughness with annealing temperature.

$AgInS_2$ annealed with Se	Before annealing	Tr = 400 °C	Tr = 450 °C	Tr = 500 °C
Roughness (nm)	31.12	182.85	152.02	213.33

The normalized absorbance spectrum $\alpha(\tilde{\lambda})$ is deuced from the relation:

$$\alpha(\tilde{\lambda}) = \frac{1}{d\sqrt[4]{2}}\cdot\sqrt[4]{\left(\ln\frac{1-R(\tilde{\lambda})}{T(\tilde{\lambda})}\right)^4 + \left(2\ln\frac{1-R(\tilde{\lambda})}{\sqrt{T(\tilde{\lambda})}}\right)^4} \quad (9)$$

where d is the layer thickness.

The obtained value of normalized absorbance spectrum $\alpha(\tilde{\lambda})$ is a final guide to the determination of the effective absorptivity $\hat{\alpha}$ through (Eq. (7)).

The Amlouk–Boubaker opto-thermal expansivity ψ_{AB} is a thermo-physical parameter defined in precedent studies [25–27], as a 3D expansion velocity of the transmitted heat inside the material. It is expressed in $m^3\ s^{-1}$, and calculated by:

$$\psi_{AB} = D/\hat{\alpha} \quad (10)$$

where D is the thermal diffusivity and $\hat{\alpha}$ is the effective absorptivity.

Values of The Amlouk–Boubaker opto-thermal expansivity ψ_{AB} of the studied films are gathered in Table 5.

3.4. Urbach tailing features

Urbach energy E_u has been determined through the equations:

$$\begin{cases} Ln(\alpha(h\nu)) = Ln(\alpha_0) + \frac{h\nu}{E_u} \\ E_u = \alpha(h\nu)\left(\frac{d[\alpha(h\nu)]}{d[h\nu]}\right)^{-1} = h\left[\frac{d}{d\nu}(Ln\alpha(\nu))\right]^{-1} \end{cases} \quad (11)$$

where $\alpha(h\nu)$ represents the experimentally deduced optical absorption profile.

The width of the localized states (band tail energy or Urbach energy E_u) has been estimated (Table 6) from the slopes of $(Ln\alpha(\nu))$ versus energy $h\nu$ plots of the films (Fig. 6).

Table 5
Values of the Amlouk–Boubaker opto-thermal expansivity ψ_{AB}.

Sample		ψ_{AB} (10^{-12} m^3 s^{-1})
Unannealed $AgInS_2$		11.58
Annealed $AgInS_2$	(Tr = 400 °C)	10.06
	(Tr = 450 °C)	9.38
	(Tr = 500 °C)	7.62

Table 6
Values of Urbach energy of $AgInS_2$ thin films.

Sample		EU (meV)
Unannealed $AgInS_2$		319.61
Annealed $AgInS_2$	(Tr = 400 °C)	291.37
	(Tr = 450 °C)	273.25
	(Tr = 500 °C)	252.17

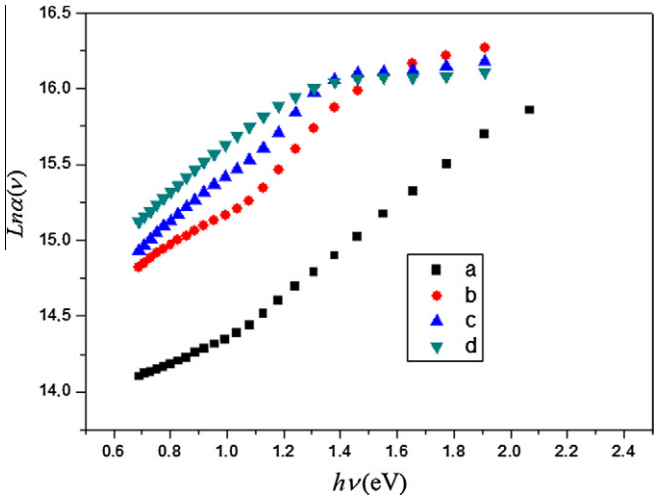

Fig. 6. Values of $Ln\alpha$ versus energy $h\nu$ plots as guides to determine Urbach energy for $AgInS_2$ (a: before annealing, b: annealed at 400 °C, c: 450 °C, d: 500 °C).

3.5. Optical characterization

We determined values of n and k from the transmittance and the reflectance spectra of the thin films. They are very weak less than 40%. The thin films are good absorber the absorbance is more 65%. After the annealing, the coefficient of transmittance and reflectance was very weak. We will calculate the absorbance A with Lambert formula:

$$\begin{cases} A = 1 - (R + T) \\ 2.303A = \alpha d \end{cases} \tag{12}$$

where h α is absorption coefficient of and d is thin film thickness ($d = 0.7 \times 10^{-6}$ m), along with the extinction coefficient k:

$$k = \frac{\alpha\lambda}{4\pi} \tag{13}$$

The spectra curves of n values determined using above relationships are shown in Fig. 7. As seen, n values increase with increasing of the wave length after the values of the energy band gap. The values of index refraction are decreasing with the increasing of the annealing temperature.

Forouhi et al. [1] has defined two expressions of the extinction coefficient k versus the energy E:

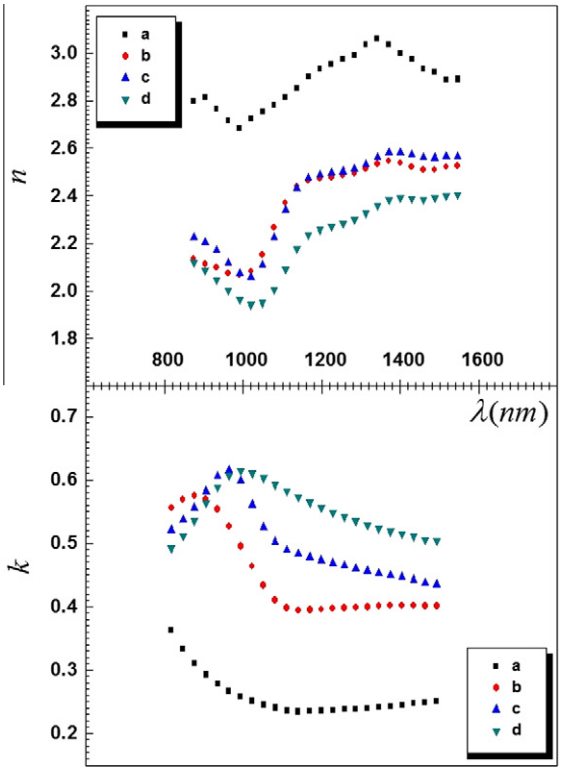

Fig. 7. Reflexion index and extinction coefficient of $AgInS_{2-x}Se_x$ (a: before annealed, b: annealed at 400 °C, c: annealed at 450 °C, d: annealed at 500 °C).

$$k(E) = \frac{A(E - E_g)^2}{(E^2 - BE + C)} \tag{14}$$

where A, B and C are positive nonzero constants characteristic of the medium such that $4C\text{-}B^2 > 0$, E_g represents the optical energy band gap. The index of refraction n is determined to be:

$$n(E) = n(\infty) + \frac{(B_0E + C_0)}{(E^2 - BE + C)} \tag{15}$$

Using Kramers–Kroning analysis, where B_0 and C_0 are constants that depend on A, B, C and E_g and $n(\infty)$ is a constant greater than unity (Table 7).

In the literature, the absorber thin films $AgInS_2$ and $AgInSe_2$ have low direct gap energies. Thus the plots of $(\alpha h\nu)^2$ versus $(h\nu)$ were performed in order to obtain the badgap energy of four thin films of $AgInS_2$ at different annealed temperatures (Table 7), as shown in (Fig. 8). Eq. (15) is determined as,

$$(\alpha h\nu)^2 = A(h\nu - E_g) \tag{16}$$

The energy band gap was determined from the linear portions as shown in figures and the values are given in Table 8. We can compare the values of energy band gap at different annealing temperatures. It is varied from 1.61 eV before annealed to 0.98 eV at annealed temperature 450 °C. It decreases with increasing of the annealing temperature. We can deduced that the effect of the annealing reduce the energy band gap. The high value of absorption coefficient α ($\alpha > 10^5$) and very large band gap energy we encouraged to use these thin film as absorber in the solar cells.

Thus, the refractive index is related to photon energy through the relation [23]:

$$n^2 = 1 + \frac{E_0E_d}{E_0^2 - (h\nu)^2} \tag{17}$$

Table 7
Different parameters of $n(E)$.

Thin films $AgInS_{2-x}Se_x$	$n(\infty)$	B_0	C_0	B	C
Tr = 400 °C	2.166	−0.179	0.211	2.583	1.771
Tr = 450 °C	2.268	−0.146	0.164	2.552	1.705
Tr = 500 °C	2.210	−0.144	0.139	2.491	1.669

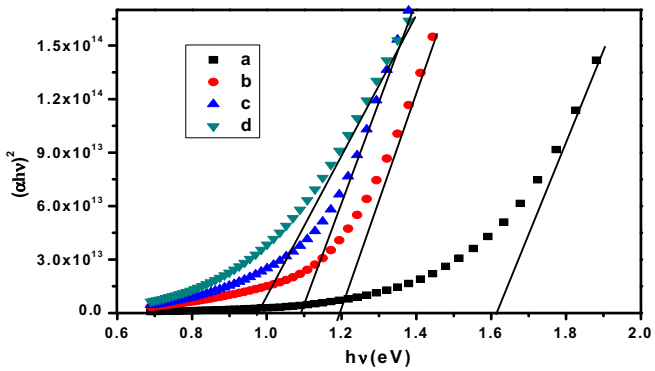

Fig. 8. The band gap of thin film $AgInS_2$ annealed with Se (a: before annealed, b: annealed at Tr = 400 °C, c: annealed at Tr = 450 °C, d: annealed at Tr = 500 °C).

Table 8
Variation of the band gap with variation of the annealed temperature.

Sample	$AgInS_2$/glass	$AgInS_2$/glass annealed with (Se)		
	Before annealing	Tr = 400 °C	Tr = 450 °C	Tr = 500 °C
Band gap (eV)	1.61	1.18	1.11	0.98

where E_0 and E_d are single-oscillator constants. Values of the most relevant parameters are gathered in Table 9. The parameter E_d is the oscillator strength of interband optical transitions. The oscillator E_0 is an average energy gap. Furthermore, an approximate value of the optical band gap, E_g can be obtained from the Wemple–Didomenico model. The optical band gap values E_g were also calculated using $E_g \approx E_0/2$ relationship. The E_g^{WD} values obtained from Wemple–Didomenico model are in agreement with those determined from the tau model (Table 9).

The long wavelength refractive index (n_∞), average interband oscillator wavelength (λ_o) and the average oscillator strength (S_o) for the thin films were determined using the following relation [23]:

$$\frac{n_\infty^2 - 1}{n^2 - 1} = 1 - \left(\frac{\lambda_0}{\lambda}\right)^2 \tag{18}$$

where (n_∞) and (λ_0)) values were calculated from the plots $(n^2-1)^{-1}$ versus λ^{-2} and are given in Table 9.

This equation can also be written as [23]:

$$n^2 - 1 = \frac{S_0\lambda_0^2}{1 - \left(\frac{\lambda_0}{\lambda}\right)^2} \tag{19}$$

where $S_0 = \frac{n_\infty^2 - 1}{\lambda_0^2}$. S_0 and E_0 values were obtained using above equation and are given in Table 9.

The complex dielectric constant $\varepsilon = \varepsilon_1 - i\varepsilon_2$ where ε_1 is the real part and ε_2 is the imaginary part of the dielectric constant. They can be written in the following form: $\varepsilon_1 = n^2 - k^2$ and $\varepsilon_2 = 2nk$.

The dependences of ε_1 and ε_2 on photon energy are shown in Fig. 9. The real and imaginary parts of follow the same pattern and it is seen that the values of real part are higher than imaginary part. The variation of the dielectric constant with the photon energy indicates that the some interactions between photons and electrons in the films are produced in the energy range.

3.6. Thermal properties

3.6.1. Principle of the mirage effect detection

The absorbing sample is heated by a modulated light beam of intensity $I = I_0(1 + \cos \omega t)$. The generated thermal wave will propagate into the sample and in the surrounding fluid and induce a temperature gradient, and will therefore lead to a refractive index gradient in the fluid. A laser probe beam crossing the fluid will undergo a deflection. To calculate this deflection, it is initially necessary to determine the temperature at the sample surface, in order to deduce the refractive index gradient in the fluid, Fig. 10. The experimental set up is described in Ref. [19].

3.6.2. Theoretical model

The theoretical model is built on the resolution of the one dimension heat equation in the different media, fluid, sample and backing by assuming the continuity of the temperature and the heat flow at the different interfaces $z = 0$ and $z = -l_s$ (Fig. 11).

We assume that both fluid and backing are optically non absorbing media for the incident light.The obtained expression of the periodic elevation temperature at the sample surface T_0 [19] given by Eq. (21) will permit the calculation of the probe beam deflection ψ [19] given by Eq. (22)

$$T_0 = -\frac{E[(1-r)(1+b)e^{(\sigma_s l_s)} - (1+r)(1-b)e^{-\sigma_s l_s)} + 2(r-b)e^{(-\alpha l_s)}]}{[(1+g)(1+b)e^{(\sigma_s l_s)} - (1-g)(1-b)e^{(-\sigma_s l_s)}]} \tag{20}$$

where $E = A/(\alpha^2 - \sigma_S^2)$, $b = K_b\sigma_b/K_s\sigma_s$, $g = K_f\sigma_f/K_s\sigma_s$ and $r = \alpha/\sigma_s$ $\sigma_i = (1+j)/\mu_i$, $\mu_i = (D_i/\pi\nu)^{1/2}$ α is the optical absorption coefficient of the sample and ν is the modulation frequency. K_i, D_i and μ_i are respectively the thermal conductivity, the thermal diffusivity and the thermal diffusion length of the i medium. Here the index i take the subscripts s, f and b, respectively, for the sample, fluid and backing

$$\Psi(z,t) = \frac{-L}{n_0}\frac{dn}{dT_f}\frac{\sqrt{2}}{\mu_f}|T_0|e^{(-z_0/\mu_f)}e^{\left[j\left(\theta+\frac{\pi}{4}-\frac{z_0}{\mu_f}\right)\right]}e^{j\omega t} \tag{21}$$

where z_0 is the distance between the probe beam axis and the sample surface.

As T_0 and ψ are complex numbers, there may be written as:

$$T_0 = |T_0|\exp(j\theta) \quad \text{and} \quad \Psi = |\Psi(z_0)|\exp(j\Phi)$$

where $|\Psi(z_0)| = -\frac{L}{n_0}\frac{dn}{dT_f}\frac{\sqrt{2}}{\mu_f}|T_0|\exp(-z_0/\mu_f)$ and $\Phi = \frac{-z_0}{\mu_f} + \theta + \frac{\pi}{4}$ are the amplitude and phase of the photothermal deflection signal

Table 9
Values of the most relevant parameters.

	E_d (eV)	E_0 (eV)	S_0 μm^{-2}	λ_0 μm	$n(\infty)$	W_p (10^{14} rad s^{-1})	τ (10^{-13} s)	N/m (10^{47} g cm^{-1})	δ
Unannealed	17.02	3.91	26	0.40	2.30	12.8	0.54	54.3	7540
400 °C	17.96	2.51	18.3	320	1.69	12.8	0.31	17.6	14200
450 °C	18.87	2.45	30.7	279	1.84	14.3	0.11	34.7	10670
500 °C	20.59	1.85	35	244	1.75	14.8	0.10	32.4	8600

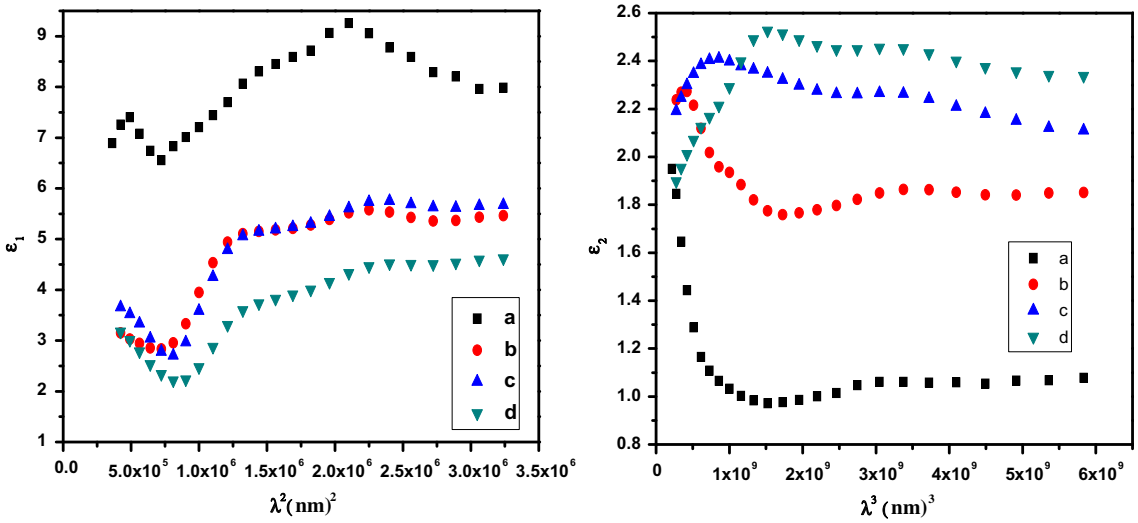

Fig. 9. Effect of heat treat for variation of ε_1 and ε_2 $AgInS_{2-x}Se_x$ (a: before annealed, b: annealed at 400 °C, c: annealed at 450 °C, d: annealed at 500 °C).

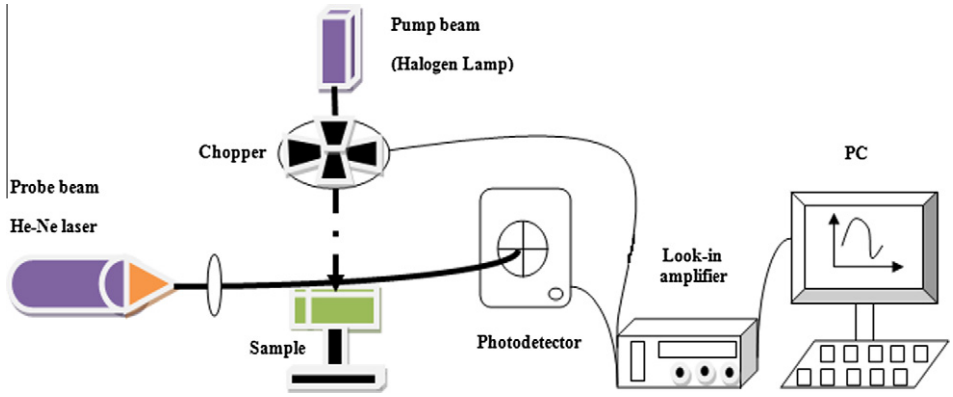

Fig. 10. Experimental set-up.

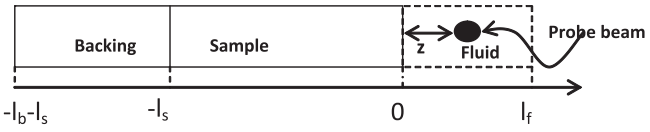

Fig. 11. Schematic representation for different media browsed by the heat.

whereas $|T_0|$ and θ are respectively the amplitude and phase of the sample's surface temperature.

3.6.3. Experimental results

The thermal conductivity K_c plays a critical role in controlling the performance and stability of materials and it is one of the main fundamental properties of materials such as density, melting point, entropy, resistance, and crystal structure parameters. Different techniques were used to determine the thermal properties such as; photo acoustic, radiometric and Mirage effect which are used in this paper to investigate the thermal conductivity of $AgInS_2$ thin film annealed with Selenium at different annealing temperatures. Fig. 12A and B despites the experimental variations of the logarithm of amplitude and the phase versus the square root of frequency for different annealed temperatures.

The variations of the curves of the logarithm of amplitude and the phase demonstrate well the changed of the thermal conductivity with the annealed temperatures.

We have in our laboratory method to determine the value of the thermal conductivity from the theoretical model and the experimental curves. The principal of this method is changed the values of the thermal conductivity to obtain the equal between the theoretical and the experimental curves. It is presented in Fig. 13A and B.

When we determined the value thermal conductivity, we applied this value for the other experimental curves of the same thin films at different position to confirm this value. It is presented in Figs. 14–17.

The curve of logarithm of amplitude and the phase varied with the annealed temperature, so that the thermal property of the thin films changed, from the literature [19], the thermal conductivity decreases with the annealing temperatures. It passes from 0.53 w/mK before annealed to 0.48 w/mk at the annealed temperature 400 °C and to 0.32 w/mk at 450 °C after this temperature the thermal property has very weak variation. It was 0.27 w/mk at 500 °C which are shown in Table 10. These values are in good agreement with those reported in [16–18]. We can deduce the thermal treatment can ameliorate the thermal conductivity and it will have very high capacity to storage more the energy solar to transform in electrical energy. So, we can use as absorber in the solar cell.

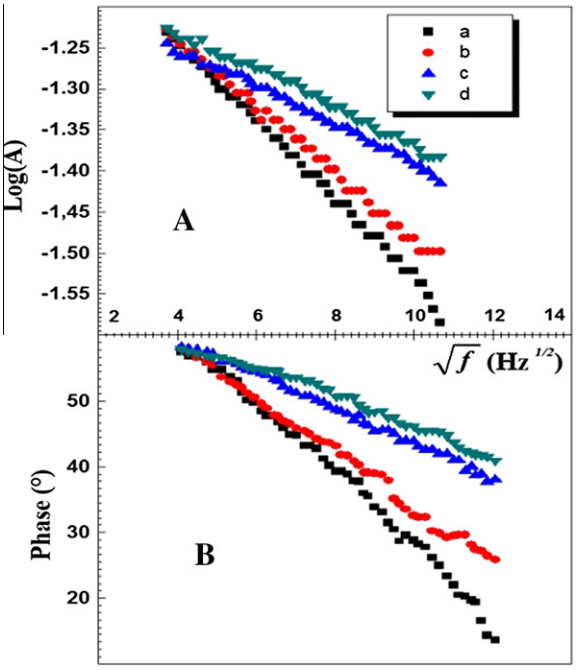

Fig. 12. (A and B) Plots of logarithm-amplitude and phase shift versus frequency square root for the thin films (a: before annealing, b: annealed at 400 °C, c: annealed at 450 °C, d: annealed at 500 °C).

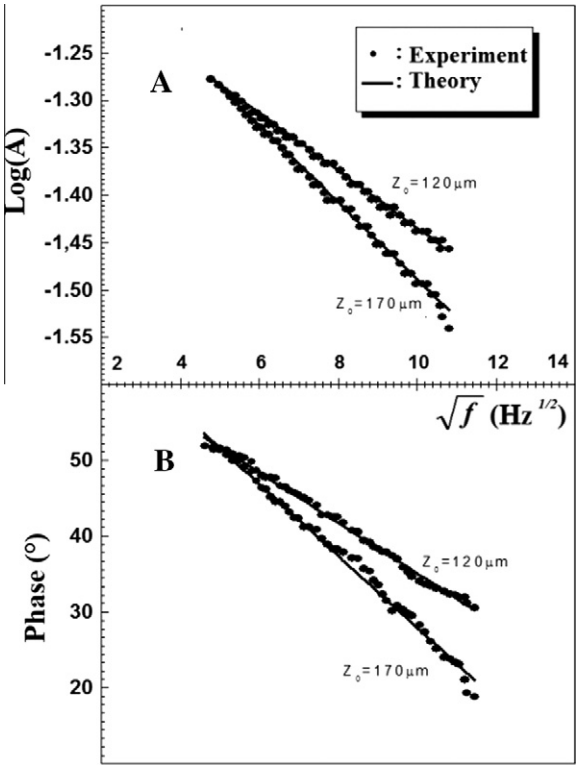

Fig. 14. (A and B) The theoretical and experimental curves of the thermal conductivity $K_c = 0.53$ w m^{-1} k^{-1} of $AgInS_2$ thin films unannealed at two different position Z_0.

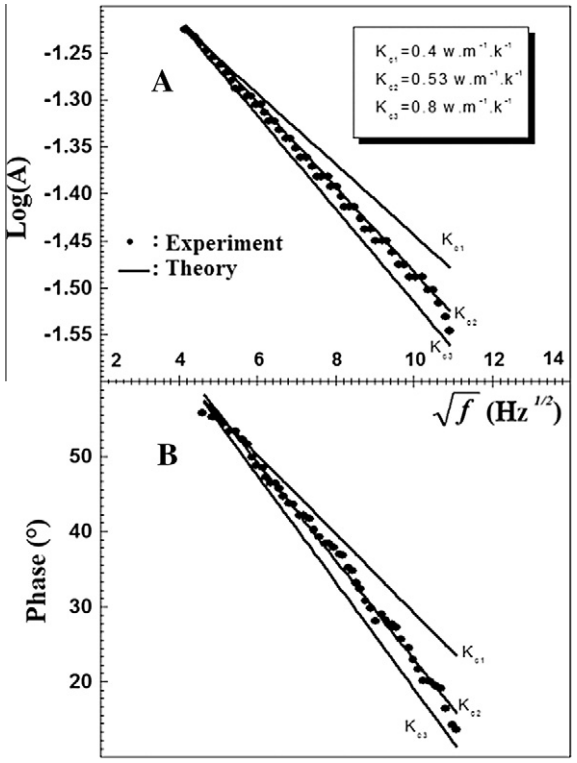

Fig. 13. (A and B) Plots of logarithm-amplitude and phase shift versus frequency square root for the different thin films and for different values of the thermal conductivity.

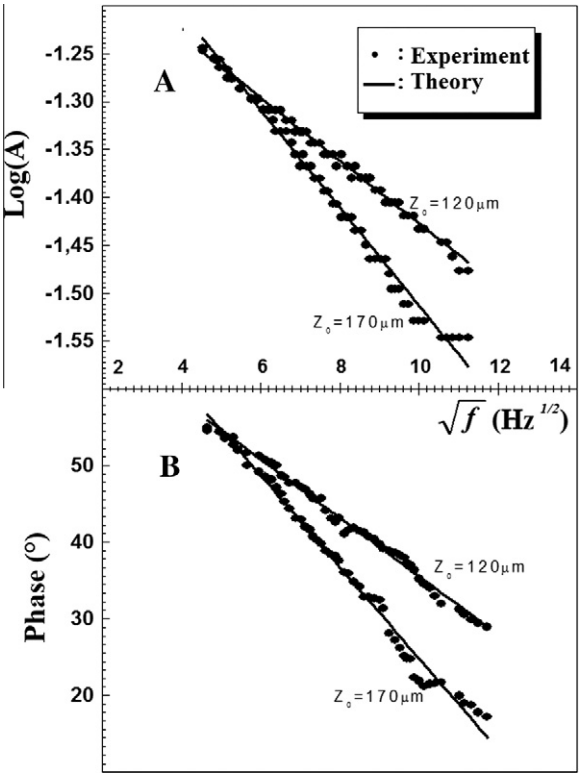

Fig. 15. (A and B) Theoretical and experimental plots of the thermal conductivity $K_c = 0.48$ w m^{-1} k^{-1} of $AgInS_2$ annealed at 400 °C with Se at two different positions Z_0.

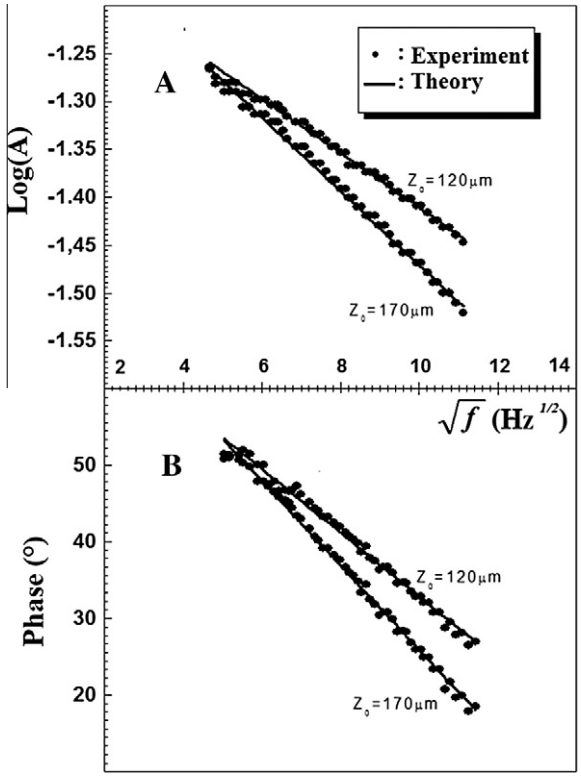

Fig. 16. (A and B) The theoretical and experimental curves of the thermal conductivity $K_c = 0.32$ w m^{-1} k^{-1} of $AgInS_2$ annealed at 450 °C with Se at two different positions Z_0.

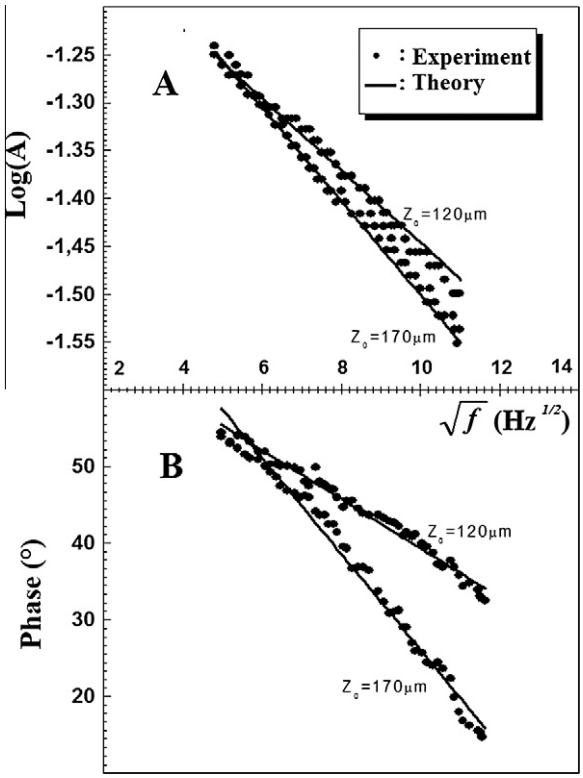

Fig. 17. (A and B) The theoretical and experimental curves of the thermal conductivity $K_c = 0.27$ w m^{-1} k^{-1} of $AgInS_2$ annealed at 500 °C with Se at two different positions Z_0.

Table 10
Values of the K_c (w m^{-1} K^{-1}) of $AgInS_2$ thin film annealed with Se.

$AgInS_2$	Unannealed	Tr = 400 °C	Tr = 450 °C	Tr = 500 °C
Thermal conductivity K_c (w m^{-1} K^{-1})	0.53	0.48	0.32	0.27

4. Conclusion

Structural and optical properties of $AgInS_{2-x}Se_x$ thin films grown by spray pyrolysis and annealed with Se at three different temperatures. The X-ray diffraction spectra indicated that the AIS films with secondary phase were successful grown by annealing above 420 °C. However, the secondary phases disappeared perfectly in the evaporated AIS films annealed with Se above 400 °C. The $AgInS_{2-x}Se_x$ grain sizes became large with increasing the annealing temperatures. Also, the thermal conductivity decreases with the annealed temperatures.

References

[1] A.R. Forouhi, I. Bloomer, Phys. Rev. B 34 (10) (1986) 7018–7022.
[2] L.K. Samanta, D.K. Ghosh, G.C. Bhar, Phys. Rev. B 33 (1986) 4145.
[3] M.A. Contreras, K. Ramanathan, J. AbuShama, F. Hasoon, D.L. Young, B. Egaas, R. Noufi, Prog. Photovolt. Res. Appl. 13 (2005) 209.
[4] Z. Aissaa, T. Ben Nasrallaha, M. Amlouka, J.C. Bernède, S. Belgacem, Sol. Energy Mater. Sol. Cells 90 (2006) 1136–1146.
[5] Z. Aissa, M. Amlouk, T. Ben Nasrallah, J.C. Bernède, S. Belgacem, Sol. Energy Mater. Sol. Cells 91 (2007) 489–494.
[6] H. Miyake, T. Haginoya, K. Sugiyama, Sol. Energy Mater. Sol. Cells 50 (1998) 51.
[7] Kenji Yoshino, Naoji Mitani, Mutsumi Sugiyama, Shigefus, F. hichibu, Hironori Komaki, Tetsuo Ikari, Physica B 302–303 (2001) 349–356.
[8] J.L. Shay, J.H. Wernick, Ternary Chalcopyrite Semiconductors: Growth, Electronic Properties and Applications, Pergamon Press, New York, 1975.
[9] Y. Akaki, S. Kurihara, M. Shirahama, K. Tsurugida, S. Seto, b.T. Kakeno, c.K. Yoshino, J. Phys. Chem. Solids 66 (2005) 1858–1861.
[10] Z. Aissa, A. Bouzidi, M. Amlouk, J. Alloys Compd. 506 (2010) 492–495.
[11] M. Ortega Lopez, Mater. Res. Bull. 38 (2003) 55–61.
[12] M. Gorska, R. Beaulieu, J.J. Loferski, B. Roessler, Thin Solid Films 67 (1980) 41–345.
[13] A.H. Ammar, A.M. Farid, M.A.M. Seyam, Vacuum 66 (2002) 27–38.
[14] M. Lopez, A. Acevedo, O. Feria, Thin Solid Films 385 (2001) 120–125.
[15] T. Ghrib, N. Yacoubi, F. Saadallah, Sensors and Actuators A 135 (2007) 346–354.
[16] L.K. Samanta, D.K. Ghosh, G.C. Bhar, Chem. Phys. 79 (1983) 361.
[17] A. Vermaa, B. Sarkarb, S. Sharmaa, R. Bhandaric, V. Jindal, Mater. Chem. Phys. 127 (2011) 74–78.
[18] M.L. Vale-Gil, C. Rincon, Mater. Lett. 17 (1993) 59–62.
[19] I. Gaied, A. Amara, N. Yacoubi, T. Ghrib, Appl. Opt. 47 (8) (2008) 1054–1062.
[20] K. Boubaker, A. Chaouachi, M. Amlouk, H. Bouzouita, Eur. Phys. J. Appl. Phys. 37 (2007) 105.
[21] K. Okamoto, K. Kinoshta, Solid-Slate Electron. 19 (1976) 31–35.
[22] S. Fridjine, S. Touihri, K. Boubaker, M. Amlouk, J. Crystal Growth (2009), http://dx.doi.org/10.1016/j.jcrysgro.2009.10.039.
[23] F. Yakuphanoglu, A. Cukurovali, I. Yilmaz, Physica B 353 (2004) 210–216.
[24] M.R. Vaezi, S.H. Mir Shah Ghassemi, A. Shokuhfar, Mater. Sci.-Poland 26(3) 2008.
[25] A. Chaouachi, K. Boubaker, M. Amlouk, H. Bouzouita, Eur. Phys. J. Appl. Phys. 37 (2007) 105.
[26] A. Amlouk, K. Boubaker, M. Amlouk, J. Alloys Compd. 490 (2010) 602–604.
[27] A. Amlouk, K. Boubaker, M. Amlouk, M. Bouhafs, J. Alloys Compd. 485 (2009) 887–891.
[28] O.D. Oyodum, O.B. Awojoyogbe, M. Dada, J. Magnuson, Eur. Phys. J.-App. Phys. 46 (2) (2009).
[29] O.B. Awojoyogbe, K. Boubaker, Curr. App. Phys. 9 (2009).
[30] J. Ghanouchi, H. Labiadh, K. Boubaker, Int. J. Heat Technol. 26 (1) (2008) 49.
[31] S. Slama, J. Bessrour, M. Bouhafs, K.B. Ben Mahmoud, Numer. Heat Transf. Part A 55 (2009) 401.
[32] S. Slama, M. Bouhafs, K. Boubaker, Int. J. Heat Technol. 26 (2) (2008) 141.
[33] S. Slama, J. Bessrour, K. Boubaker, M. Bouhafs, Eur. Phys. J.-A. P. 44 (2008) 317.
[34] S. Slama, J. Bessrour, K. boubaker, M. Bouhafs, Proc. COTUME'08 (2008) 79.
[35] S. Fridjine, M. Amlouk, Mod. Phys. Lett. B 23 (2009) 2179.
[36] S. Fridjine, K. Boubaker, M. Amlouk, Can. J. Phys. 87 (2009) 653.
[37] S. Fridjine, K.B. Mahmoud, M. Amlouk, M. Bouhafs, J. Alloys Compd. 479 (2009) 457.
[38] S. Tabatabaei, T. Zhao, O. Awojoyogbe, F. Moses, Heat Mass Transf. 45 (2009) 1247.
[39] A. Belhadj, O. Onyango, N. Rozibaeva, J. Thermophys. Heat Transf. 23 (2009) 639.

[40] H. Labiadh, J. Diff. Eq. C. Proc. 1 (2007) 172.
[41] K. Boubaker, Trends Appl. Sci. Res. 2 (2007).
[42] K.B. Ben Mahmoud, J. Thermoph. Heat Transf. 23 (2009) 409.
[43] K. Boubaker, Int. J. Heat Technol. 20 31 (2008).
[44] T.G. Zhao, Y.X. Wang, K.B. Ben Mahmoud, Int. J. Math. Comput. 1 (2008) 13.
[45] T. Ghrib, K. Boubaker, M. Bouhafs, Mod. Phys. Lett. B 22 (2008) 2907.
[46] K. Boubaker, Far East J. Appl. Math. 31 (2008).
[47] N. Guezmir, T. Ben Nasrallah, K. Boubaker, M. Amlouk, S. Belgacem, J. Alloys Compd. 481 (2009) 543.